Journal of Materials Science: Materials in Electronics (2019) 30:13708–13718
https://doi.org/10.1007/s10854-019-01752-9

Study on photocatalytic and impedance spectroscopy investigations of composite CuO/ZnO nanoparticles

Mohamad S. AlSalhi[1] · A. Sakthisabarimoorthi[2] · Sandhanasamy Devanesan[3] · S. A. Martin Britto Dhas[2] · M. Jose[2]

Received: 20 March 2019 / Accepted: 24 June 2019 / Published online: 26 June 2019

Abstract
This paper reports the preparation of composite CuO/ZnO nanoparticles by facile precipitation route and their photocatalytic activity against organic dyes. The red shift caused in the UV–Vis absorption spectrum suggests the enhancement of visible light photocatalytic activity of the material. The collective vibrations of Cu–O and Zn–O in FTIR spectrum clearly illustrate the formation of composite CuO/ZnO nanoparticles. Powder XRD profile suggests the formation of highly crystalline material and the chemical states of the elements is investigated by XPS analysis. A slightly agglomerated cluster-like structure of the particles is visualized by SEM analysis and EDS mapping illustrates the homogeneous distribution of the sample, which is most favorable for the photocatalysis analysis. The photocatalytic activity of material is studied against degradation of Rhodamine B and Methylene blue dyes using simulated solar light irradiation. The dielectric analysis of the composite CuO/ZnO nanoparticles demonstrates the enhanced dielectric permittivity and low loss factor in comparison with pure CuO and ZnO nanoparticles.

1 Introduction

Nowadays, realizing high photocatalytic activity against organic dyes and high degradation of industrial waste water pollutants by semiconductor based nanomaterials as catalyst remains a highly prioritized area of research across the world. Interestingly, simple metal oxide nanomaterials such as TiO_2 are predominately used for the photocatalytic activity owing to their environmental friendly feature, cost-effectiveness, non-toxicity and high photosensitivity [1]. More recently, creation of composite nanomaterials by coupling two or more material has gained much interest among the scientific community due to its effective way for achieving improved physical and chemical properties than that of simple nanomaterials [2–8]. Among them, copper oxide nanoparticles (CuO NPs, p-type semiconductor having narrow energy gap of 1.2–2.4 eV) and Zinc oxide nanoparticles (ZnO NPs, n-type semiconductor having wide energy gap about 3.4 eV) have attracted attention among scientists and researchers due to their unusual and excellent properties [9–15]. Interestingly, the narrow energy gap of CuO NPs could instantly absorb visible light fascinating visible light photocatalytic activity though their unstable nature in aqueous solution hampers photocatalysis. Nevertheless, the wide energy gap of ZnO NPs could absorb the large portion of UV light and they have superior photocatalytic activity and stability against photocorrosion [16, 17]. Furthermore, CuO NPs and ZnO NPs have desirable band edge position (i.e. both conduction and valence band of CuO NPs lies over the ZnO NPs) which can thermodynamically favor the excited electrons and holes transfer among them [18]. The quantum chemical study, density functional theory and kinetic model also suggest the most favorable circumstances for the coupling of these two elements [19–21]. Hence, coupling of these two materials into one is an effective way to enhance the photocatalytic efficiency in visible region.

Besides, both the CuO NPs and ZnO NPs are well known materials for not only in photocatalyst against organic dyes but also used in the wide range of applications including, solar cells, sensors, optoelectronic devices, antibacterial activity, photoelectrochemical water splitting, and so on

✉ M. Jose
jose@shctpt.edu

[1] Research Chair in Laser Diagnosis of Cancers, College of Science, King Saud University, Riyadh 11451, Kingdom of Saudi Arabia

[2] Department of Physics, Sacred Heart College (Autonomous), Tirupattur, Tamil Nadu, India

[3] Department of Physics and Astronomy, College of Science, King Saud University, Riyadh 11451, Kingdom of Saudi Arabia

[9, 22]. In view of this, several synthesis protocols such as, reflux condensation technique [18], hydrothermal method [23], microwave assisted urea-nitrate combustion technique [24], gas controlled photo-deposition method [25], co-precipitation technique [26] and chemical vapour deposition technique [27] were developed to synthesis composite CuO/ZnO NPs, though these synthesis techniques have their own advantages as well as disadvantages.

In this perspective, composite CuO/ZnO NPs are prepared by facile precipitation route and used as photocatalyst against organic dyes such as Rhodamine B and Methylene blue. The optical and functional properties of the material are investigated by UV–Vis spectroscopy and FTIR spectroscopy, respectively. The crystal structure and chemical composition of the material is analyzed by powder XRD analysis and XPS spectroscopy. The morphology and homogeneous distribution of the elements are examined by FESEM and elemental mapping analysis. The composite CuO/ZnO NPs was used for the photocatalytic degradation against organic dyes using simulated solar light irradiation and the maximum degradation efficiency of 98.07% and 96.63% was achieved for Methylene Blue and Rhodamine B respectively at 150 min period of irradiation time. The dielectric behaviour of the sample was investigated by impedance spectroscopy over the wide frequency (1 Hz–1 MHz) at various temperatures (30–300 °C). The composite CuO/ZnO NPs exhibit quite high dielectric permittivity ($\varepsilon_r = 127$) and low dielectric loss ($\tan\delta = 0.80$) than the CuO and ZnO NPs at room temperature.

2 Materials and methods

2.1 Materials

The following reagents (Analytical grade) are used for the preparation of composite CuO/ZnO nanoparticles: Copper (II) Sulfate Pentahydrate ($CuSO_4{\cdot}5H_2O$), Zinc Nitrate Hexahydrate ($(ZnNO_3)_2{\cdot}6H_2O$), Sodium Hydroxide (NaOH). High purity deionized water was used for the preparation of all the aqueous solutions.

2.2 Preparation of composite CuO/ZnO nanoparticles

Initially, bare CuO and ZnO NPs were prepared by simple precipitation method. In brief, 15 mL of 0.67 M NaOH aqueous solution is drop wise added into 15 mL of 0.067 M $CuSO_4{\cdot}5H_2O$ solution with continuous stirring at 80 °C for 12 h. After the addition of NaOH, the colour of the solution is changed from blue into dark brown caused by the formation of CuO NPs. The solid product was harvested from the aqueous solution through the repeated washing process and then it was dried in oven at 120 °C for 10 h. In a very similar way ZnO NPs are prepared by adding 20 mL of 0.2 M NaOH aqueous solution drop wise into 20 mL of 0.1 M $(ZnNO_3)_2{\cdot}6H_2O$ solution with constant stirring for 12 h. While stirring colour of the solution is turned from colourless into white and finally it turns into milky white in colour. After repetitive washing process, the harvested sample was dried in hot air oven at 120 °C for 10 h before it was calcinated at 500 °C for 3 h.

The composite CuO/ZnO NPs were prepared by the following synthesis route: 0.1 M $(ZnNO_3)_2{\cdot}6H_2O$ salt is added into 20 mL (5 mg) of as prepared CuO NPs solution with ultrasonication of about 30 min. After the ultrasonication process, 20 mL of 0.2 M NaOH aqueous solution is gradually injected into the mixed solution under constant stirring for 12 h. Subsequently, the sample is rinsed several times with both ethanol and water to remove the untreated NO_3^- compounds and other impurities. In the end, the sample was dried in oven at 120 °C for 10 h before it was calcinated at 500 °C for 3 h.

2.3 Characterization methods

The UV–Visible spectroscopy (Cary Varian-50 LS spectrometer) was used to examine the optical behaviour of the samples over the wavelength 200–800 nm. The energy gap (Eg) of the sample was estimated according to the Tauc's equation: $(\alpha h\upsilon)^2 = A(h\upsilon - E_g)^n$, where, α, h, υ, A, and E_g are the absorption coefficient, Planck's constant, frequency, photon energy independent constant, energy gap and n is taken as ½ for direct band gap material and 2 for indirect band gap material. Fourier transform infrared spectroscopy (Cary-60 FTIR Spectrometer) was employed to investigate the coordination environment and the presence of functional groups in the samples over the wavenumber 400–4000 cm^{-1}. Powder XRD analysis (Rigaku ultima III XRD diffractometer) was used to study the crystallinity and composition of the samples over the wide angle 20°–70°. The average crystallite size of the samples was obtained by Scherrer's formula: $D = K\lambda/\beta\cos\theta$, where, D, K, λ, β and θ are the crystallite size, shape factor (0.9), wavelength of the source, Full width at half maximum and diffraction angle, respectively. X-ray photoelectron spectroscopy (PHI 5000 Versa probe scanning esca microprobe, USA with Al k-alpha radiation) was used to elucidate the core level electronic states of the elements and composition of the sample. High-resolution scanning electron microscope with an energy dispersive X-ray spectrometer (EDS) (FEI QUANTA FEG-200) was used to visualize the particles size, morphology and corresponding elemental mapping of the samples. The photocatalytic activity of the material was investigated against Rhodamine B and Methylene blue dyes using simulated solar light irradiation which is monitored by UV–Vis spectrometer (Cary-60

FTIR Spectrometer). A Halogen lamp of 500 W is used as a source of visible light irradiation which is suspended above the stirring solution about 30 cm in distance. To facilitate the adsorption/desorption equilibrium condition, the solutions were constantly stirred in dark about 30 min before exposure to the irradiation. The rate of decolorization percentage was calculated using Beer–Lambert relation: $D(\%) = [(C_0 - C_t)/C_0] \times 100\%$, where, C_0 and C_t are the concentration of the dyes at different time intervals. Impedance analyzer (PSM 1735 LCR meter at an oscillation voltage of 2 V) was used to investigate the dielectric properties of the sample over the broad frequency range (1 Hz–1 MHz) at a range of temperatures (30–300 °C).

3 Results and discussion

Figure 1a–c represents the UV–Vis absorption spectra and inset gives Tauc plot of CuO NPs, ZnO NPs and composite CuO/ZnO NPs. The typical characteristic absorption peaks centered at 293 nm, 380 nm and 389 nm correspond to the CuO NPs, ZnO NPs and composite CuO/ZnO NPs, respectively. The absorption peaks of CuO NPs and ZnO NPs are in very good agreement with the previous literature reports [17, 28]. The inclusion of ZnO NPs into CuO NPs caused significant red shift in the absorption spectrum while the absorption peak of CuO is completely vanished, which may be due to the creation of core–shell structured composite CuO/ZnO NPs. The red shift in absorption spectrum is advantage to the enhancement of visible light photocatalytic activity [29]. The energy gap (Eg) of CuO NPs, ZnO NPs and composite CuO/ZnO NPs estimated from the absorption spectra using Tauc's equation are 1.94 eV, 2.62 eV and 2.12 eV, respectively [30]. The lower energy gap and near visible region absorption of the composite CuO/ZnO NPs suggest that it could be a useful material for visible light driven photocatalyst. Figure 1d shows the FTIR spectra of CuO NPs, ZnO NPs and composite CuO/ZnO NPs, respectively. The absorption peaks emerged at the wavenumber region from 400 to 700 cm^{-1} corresponds to the presence of various metal-oxides vibrations. The peaks appeared in the FTIR spectrum of CuO NPs at 492 and 613 cm^{-1} are ascribed to the Cu–O vibrations, while the peaks appeared in the FTIR spectrum of ZnO NPs at 414 and 659 cm^{-1} are

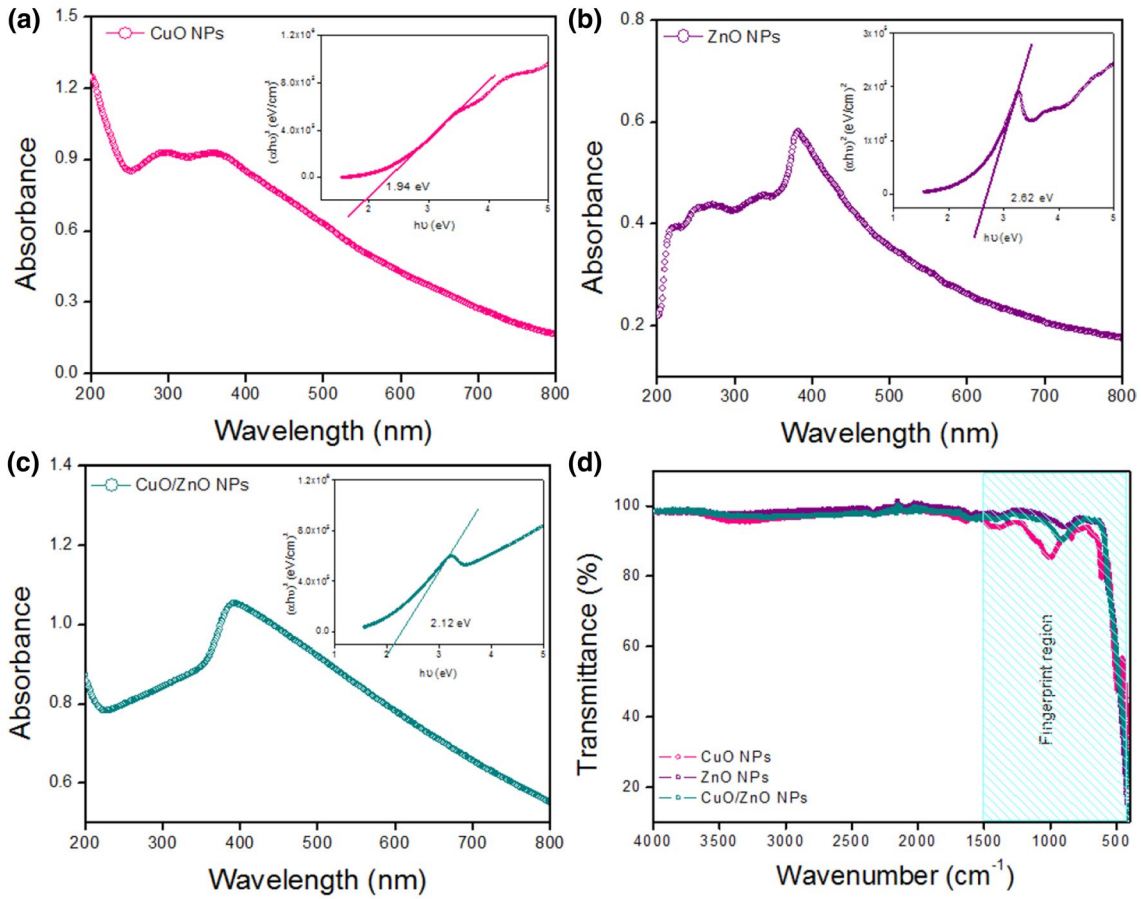

Fig. 1 **a–d** UV–Vis (inset- corresponding Tauc plot) and FTIR spectra of CuO NPs, ZnO NPs and composite CuO/ZnO NPs

attributed to the Zn–O vibrations, which indicates the formation of CuO and ZnO NPs, The absorption peak emerged in the FTIR spectrum of composite CuO/ZnO NPs at 418 and 497 cm^{-1} are assigned to the collective vibrations of Zn–O and Cu–O, which indicates the formation of composite CuO/ZnO NPs [17]. Besides, it is observed from all the three spectra that there are no traces of adsorbed water molecules being in the product at the wavenumber range of 3000 to 3500 cm^{-1}, which suggest the high purity of the products [17, 31].

Figure 2a illustrates the powder XRD profile of CuO NPs, ZnO NPs and composite CuO/ZnO NPs, respectively. It is clear from the CuO NPs profile, the diffraction peaks centered at the Bragg's angles 35.59°, 38.85°, 49.10°, 61.56°, 66.28° and 75.18° correspond to (002), (111), (20-2), (11-3), (310) and (22-2) crystalline planes affirmed the monoclinic structure of Copper oxide (JCPDS# 48-1548). Besides, the XRD profile of the ZnO NPs shows strong diffraction peaks at 31.90°, 34.44°, 36.31°, 47.75°, 56.80°, 63.03°, 68.10° correspond to (100), (002), (101), (102), (110), (103) and (112) crystalline planes which confirmed the hexagonal wurtzite structure of Zinc Oxide (JCPDS# 36-1451). Interestingly, the powder XRD profile of composite CuO/ZnO NPs exhibits only one set of reflection peaks associated with ZnO positions with no traces of reflection peaks corresponds to the CuO, which may be due to the formation of core–shell structured composite CuO/ZnO NPs. Furthermore, no additional reflection peaks are observed in all the three diffraction patterns which suggest the formation of pure phase of CuO NPs, ZnO NPs and composite CuO/ZnO NPs. Moreover, the average crystallite size of the sample is estimated from the Scherrer's formula is found to be 10 nm, 21 nm and 16 nm for CuO NPs, ZnO NPs and composite CuO/ZnO NPs, respectively. Figure 2b–d represents the wide angle and high-resolution XPS spectra of composite CuO/ZnO NPs. The wide scan XPS spectrum (Fig. 2b) shows that the peaks centered at 12 eV, 90.4 eV, 141.6 eV, 1023.2 eV, 1045.6 eV and 532 eV corresponds to Zn 3d, Zn 3p, Zn 3s, Zn $2p_{3/2}$, Zn $2p_{1/2}$ and O 1s states respectively which suggest the composite CuO/ZnO NPs mainly exist in the form of ZnO, which substantiates the core–shell structure of the product. Since, when the thickness of shell material produced is relatively

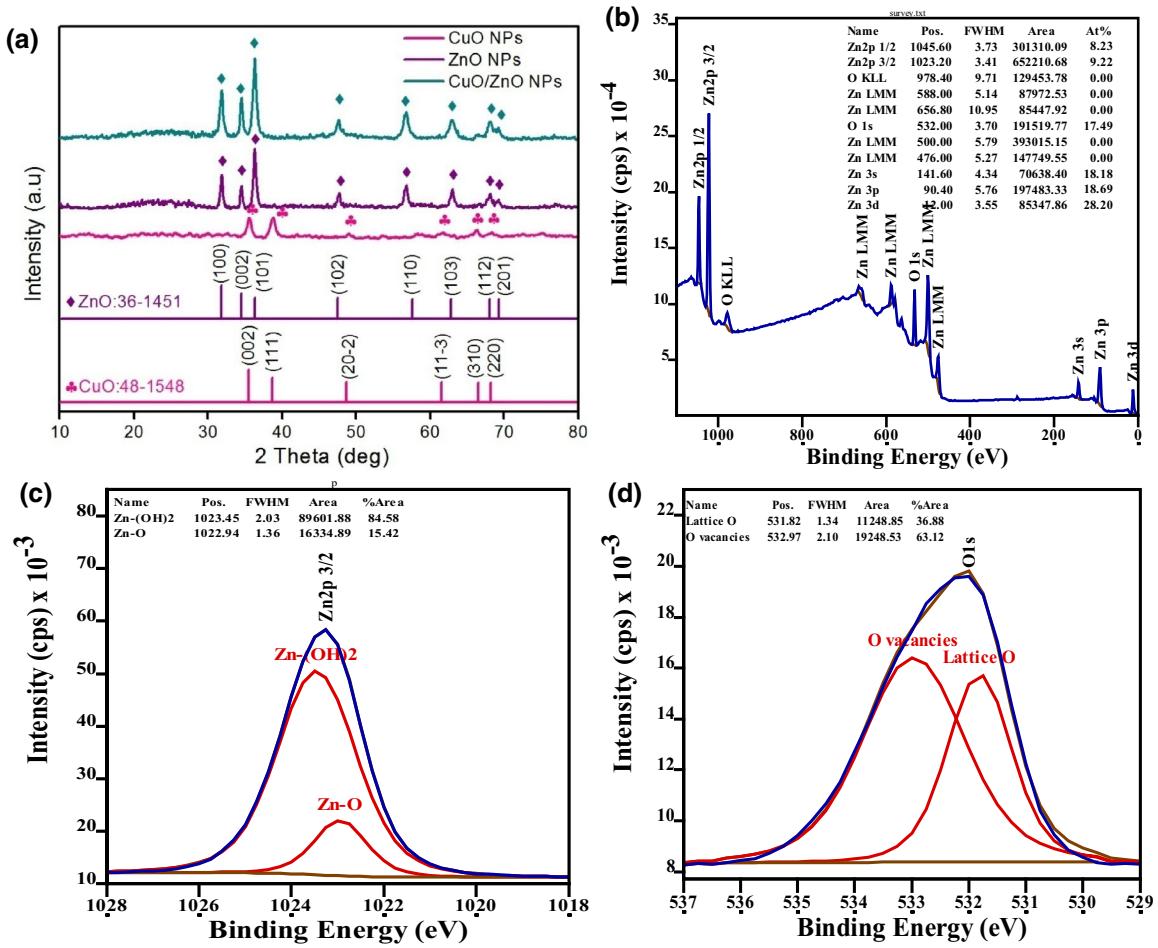

Fig. 2 **a** powder XRD pattern of CuO NPs, ZnO NPs and composite CuO/ZnO NPs; **b–d** XPS spectra of composite CuO/ZnO NPs

higher than the core, XPS spectra may not give the profile of core material due to the detection limit of the probe. Figure 2c shows the high-resolution XPS spectrum of Zn $2p_{3/2}$ state; the two deconvoluted Gaussian peaks located at the binding energy of 1022.9 eV and 1023.4 eV is due to associated Zn–O and Zn-$(OH)_2$ species, respectively [32]. Figure 2d gives the high-resolution spectrum of O 1 s state which shows two deconvoluted peaks centered at 531.8 eV, 532.9 eV due to lattice oxygen and oxygen vacancies in metal oxide (ZnO) [33]. This XPS result confirms the creation core–shell structured composite CuO/ZnO NPs, which is in good harmony with the powder XRD results.

Figure 3a–d shows the HRSEM images of CuO NPs, ZnO NPs and composite CuO/ZnO NPs, respectively. The morphology of the CuO NPs exhibits a dart-like structure rather than the typical spherical structure (Fig. 3a) whereas the ZnO NPs exhibits a typical spherical morphology (Fig. 3b). The addition of ZnO NPs into the CuO NPs caused significant change in morphology of the composite CuO/ZnO NPs such that the ZnO particles are fairly tethered on the dart-like CuO structure and exhibits slightly agglomerated cluster-like structure (Fig. 3c, d). In order to elucidate the elemental composition and surface homogeneity of the elements in the composite CuO/ZnO NPs, EDS elemental mapping was recored (Fig. 4a–f). The overlay image gives the homogeneous distribution of composite CuO/ZnO NPs over large areas such as, Cu, Zn and O elements. The quantity of distributed Zn element is typically larger compared to the Cu element which suggest that the surface of the product is mostly tethered by ZnO NPs rather than CuO NPs. The homogeneous distribution of the product is most favorable for the photocatalytic activity. Furthermore, as can be seen from the EDS spectrum, no other noticeable chemical species are detected other than Cu, Zn and O elements and the atomic percentages of CuO NPs (2.69%) is extremely lower than that of ZnO NPs (63.60%) (Fig. 4f).

Figure 5a, b gives the variation in absorption spectra of Rhodamine B and Methylene blue dyes by composite CuO/ZnO NPs under simulated solar light irradiation for various exposure times. The 0.10 g of catalyst was added into the 50 mL of each dye solutions, wherein the concentration of the dyes are taken as 10 ppm. Before irradiation of light, the high intensity absorption peak of Methylene Blue and Rhodamine B are positioned at 664 nm and 553 nm, while during the regular increment of irradiation time; the peak intensity is gradually decreased and completely vanished after 150 min period of irradiation time. Consequently, the colour of the solution changed from blue to pink into colorless due to the degradation of Methylene Blue and Rhodamine B dyes by composite CuO/ZnO NPs. The minor extent

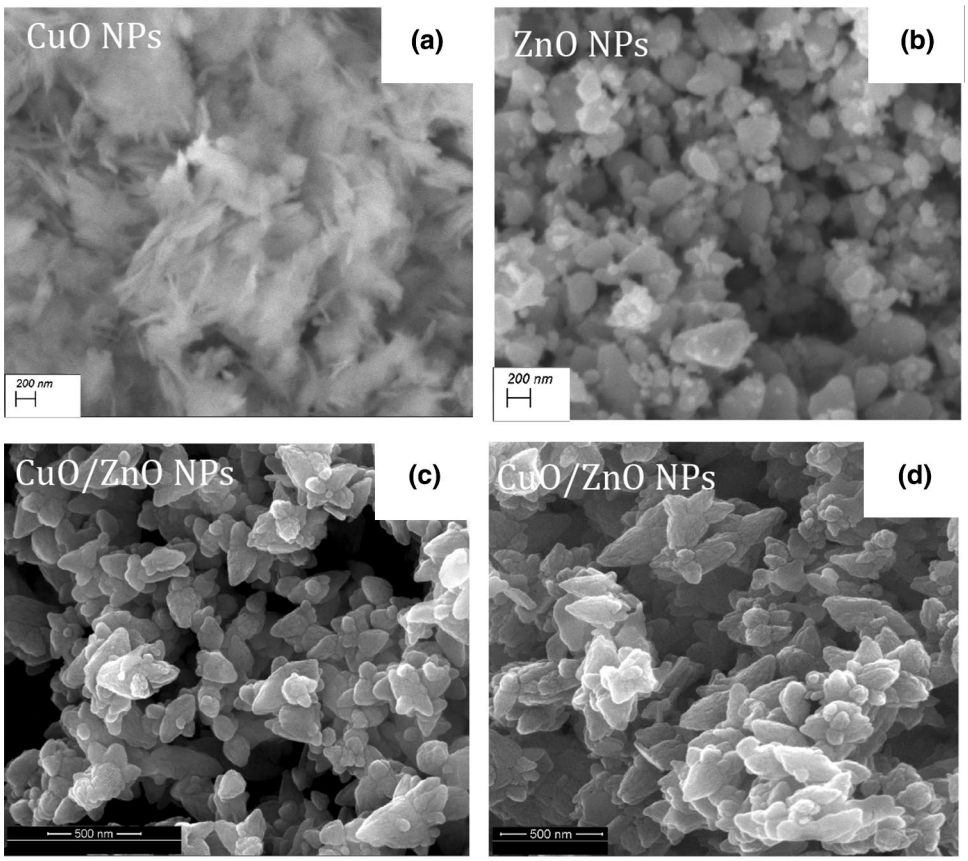

Fig. 3 **a**, **b** HRSEM images of CuO NPs and ZnO NPs; **c**, **d** composite CuO/ZnO NPs

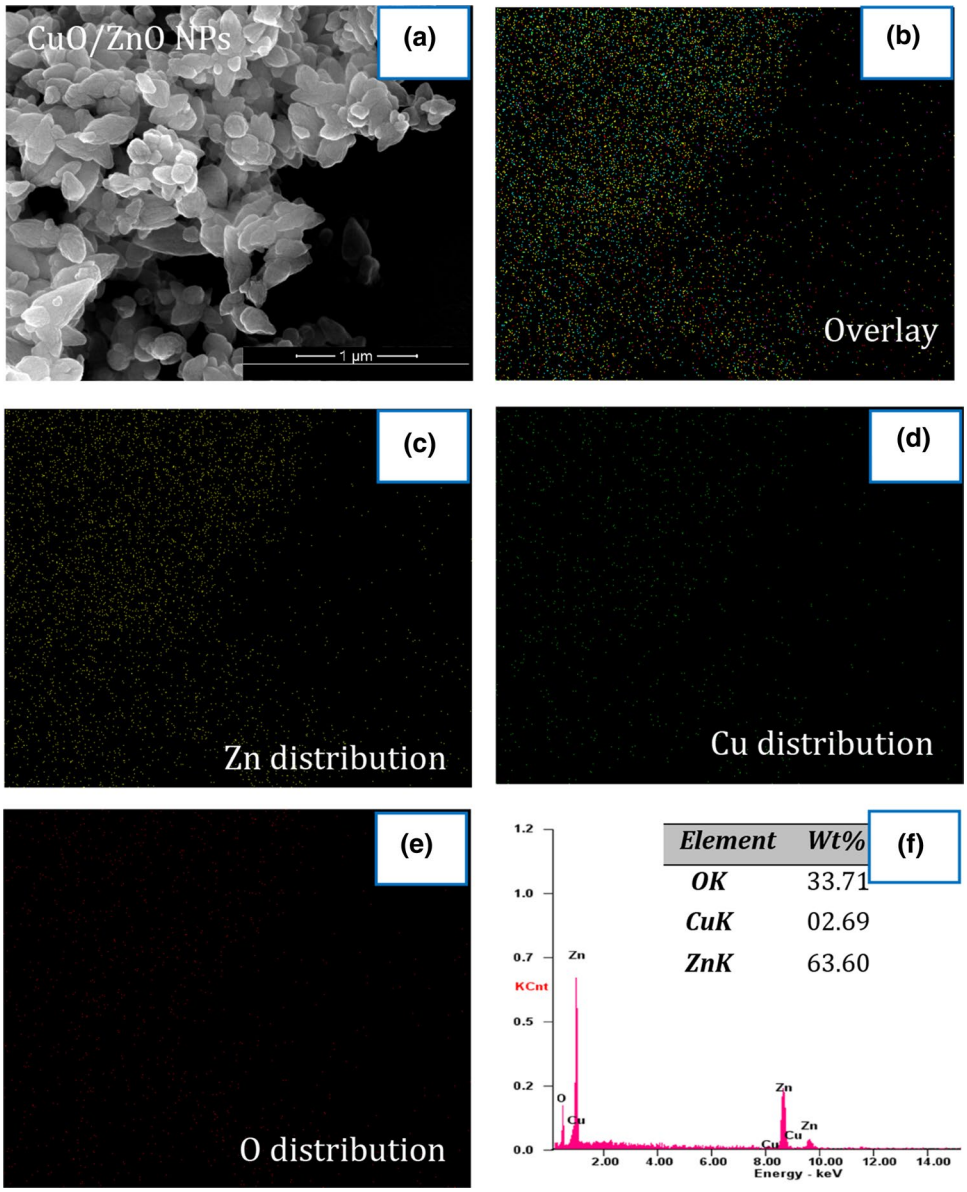

Fig. 4 **a–f** EDS elemental mapping of composite CuO/ZnO NPs

of degradation obtained 40% at 30 min irradiation time may be due to the RhB molecules adsorbed on the surface of the composite CuO/ZnO active sites which hardly react with the hydroxyl radicals produced on the catalyst surface when compared to higher irradiation time (98% at 150 min irradiation time). Furthermore, the synergistic effect of CuO/ZnO composite is predominant at higher irradiation time due to the efficient charge separation generation to perceive the high degradation efficiency [22].

Moreover, the decolorization percentage was calculated for both organic dyes and the maximum degradation efficiency of 98.07% and 96.63% was achieved for Methylene Blue and Rhodamine B at 150 min period of irradiation time. The possible photocatalytic mechanism is described based on the previous literature reports [9, 29]. When the simulated solar light is irradiated to the sample, the electron transfer may take place from the valence band of CuO to valence band ZnO, conversely the hole transfer may take place from the valence band of ZnO to valence band of CuO. This heterojunction creation of the composite material may possibly enhance the photocatalytic degradation against organic dyes. The conduction band (E_{cb}) and valence band (E_{vb}) potentials of the CuO NPs, ZnO NPs and composite CuO/ZnO NPs at the point zero charge can be calculated by the following formula [29, 34]:

$$E_{vb} = X - E_c + 0.5E_g \quad (1)$$

$$E_{cb} = E_{vb} + E_g \quad (2)$$

where, E_{vb} and E_{cb} are the valence band and conduction band potentials respectively. Furthermore, X is the

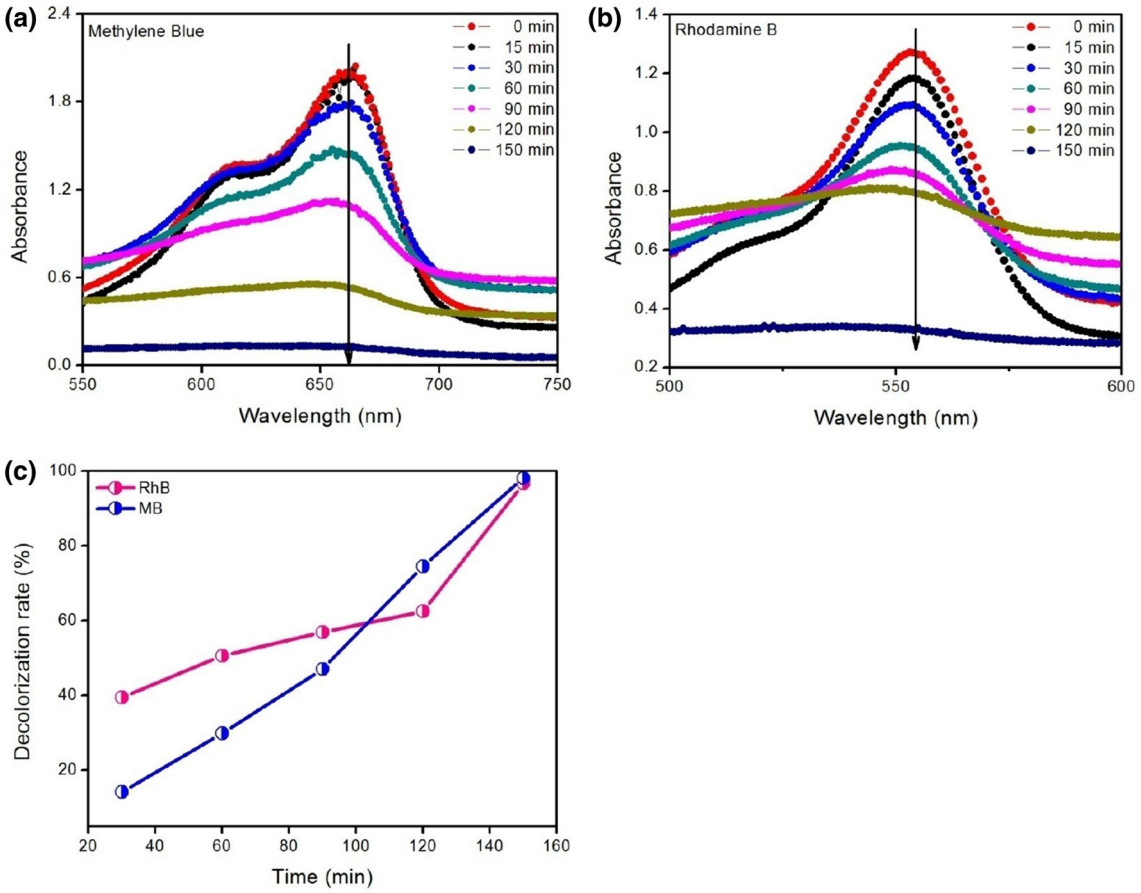

Fig. 5 **a**, **b** Photodegradation of Methylene Blue and Rhodamine B dyes by composite CuO/ZnO NPs for various time intervals **c** Decolorization rate of dyes

electronegativity of the semiconductor (X for CuO and ZnO are 5.81 eV and 5.71 eV respectively), E_c is the energy of the free electrons on the hydrogen scale (4.5 eV) and E_g is energy gap of the material. The calculated E_{vb} values are − 0.320 eV, − 0.020 eV and − 0.230 eV and the calculated E_{cb} values are 1.62 eV, 2.6 eV and 1.89 eV for CuO, ZnO and composite CuO/ZnO, respectively. The plausible photocatalyst mechanism is explained based on the following equations and the graphical representation (Fig. 6) clearly illustrates the different mechanism involved for degradation of organic dyes:

$$\mathrm{CuO}(h^+ + e^-)/\mathrm{ZnO}(h^+ + e^-) + h\upsilon = \mathrm{CuO}(h^+ + h^+)/\mathrm{ZnO}(e^- + e^-) \quad (3)$$

$$\mathrm{CuO}(h^+) + \mathrm{H_2O} \rightarrow \mathrm{OH^0} + \mathrm{H^+} \quad (4)$$

$$\mathrm{ZnO}(\mathrm{e^-}) + \mathrm{O_2} \rightarrow \mathrm{O_2^{0-}} \quad (5)$$

$$\mathrm{OH^0} + \text{Organic dyes} \rightarrow \text{Intermediates} \rightarrow \text{Degraded products} \quad (6)$$

The dielectric permittivity and loss factor of CuO NPs, ZnO NPs and composite CuO/ZnO NPs is represented in Fig. 7a. Interestingly, the dielectric permittivity of the composite CuO/ZnO NPs shows relatively high value and in contrast loss factor gives very low value at lower frequencies than that of CuO and ZnO NPs. The analogous Nyquist plot affirms the change in permittivity in terms of increase in conduction of the material (Fig. 7a). The radius of the semicircular arc is extremely decreased, which indicates an increase in conduction with corresponding decrease in charge transfer resistance of the composite CuO/ZnO NPs in comparison with CuO NPs and ZnO NPs [35]. This variation in dielectric property of the material is mainly associated with the addition of ZnO NPs into CuO NPs. The change in dielectric parameters at 100 Hz and 30 °C is given in Table 1. In order to further understand the electrical behaviour of the composite CuO/ZnO NPs which is subjected to varying temperature ranging from 30–300 °C.

Figure 8a, b demonstrates the temperature dependence of the dielectric permittivity and loss spectra of the composite CuO/ZnO NPs. The dielectric permittivity is found

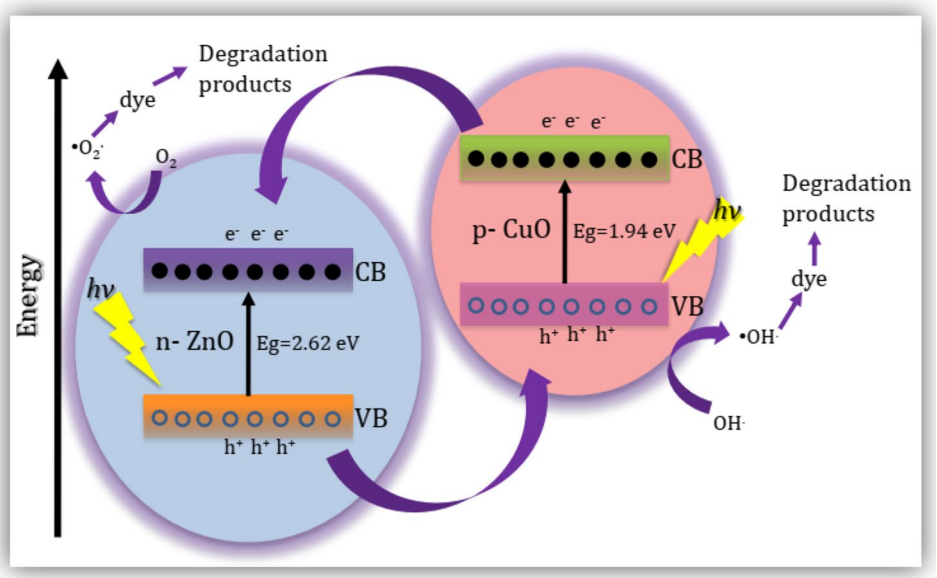

Fig. 6 Schematic representation of different mechanism involved for degradation of organic dyes using composite CuO/ZnO NPs

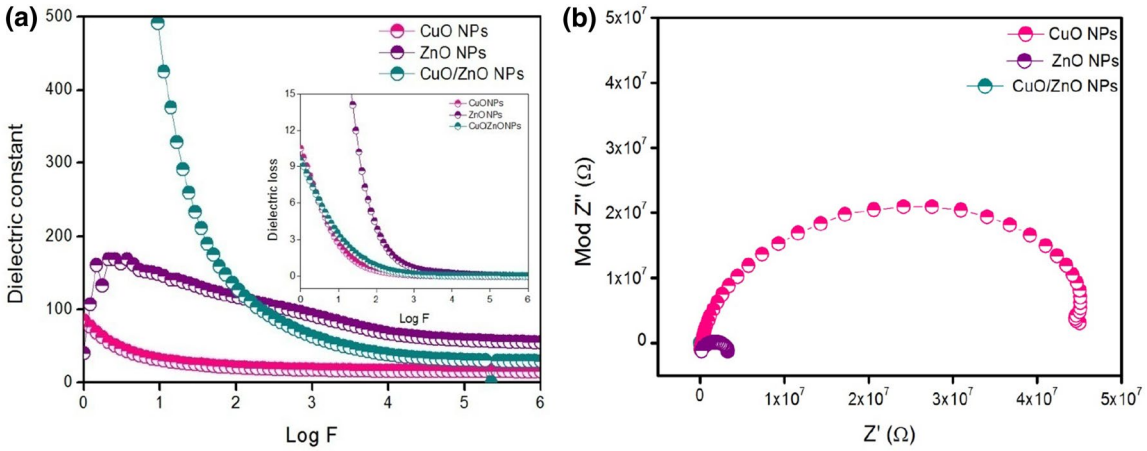

Fig. 7 **a**, **b** Dielectric permitivity (inset- loss factor) and Nyquist plots of CuO NPs, ZnO NPs and composite CuO/ZnO NPs

Table 1 Dielectric parameters of CuO NPs, ZnO NPs and composite CuO/ZnO NPs at 100 Hz and 30 °C

Sample	Dielectric permittivity	Loss factor
CuO NPs	20	0.48
ZnO NPs	116	3.82
CuO/ZnO NPs	127	0.80

to increase as the temperature is increased at low frequency regime, whereas it remains nearly constant at high frequency regime caused by the space charge polarization. The increase in rate of hopping and mobility of charge carriers greatly increase the dielectric polarization resulting in high permittivity. The emergence of peaks at higher temperatures in the loss spectra is attributed to the relaxation from the composite CuO/ZnO NPs. Besides, the electrical relaxation in the material might be associated with the freezing of electrons or activation process, which also suggests the Debye-like relaxation behaviour [36]. This indicates both the temperature and frequency dependent electrical behaviour of the material.

Figure 9a, b gives the change in real (Z′) and imaginary part (Z″) of impedance at varying temperatures. The magnitude of Z′ gradually decreases with increase in temperature at low frequency regime and remains unchanged at high frequency regime, which suggests an increase in electrical conduction of the material. This typical trend is attributed to the possible release of space charge and letting down barrier properties of the material [37]. On the

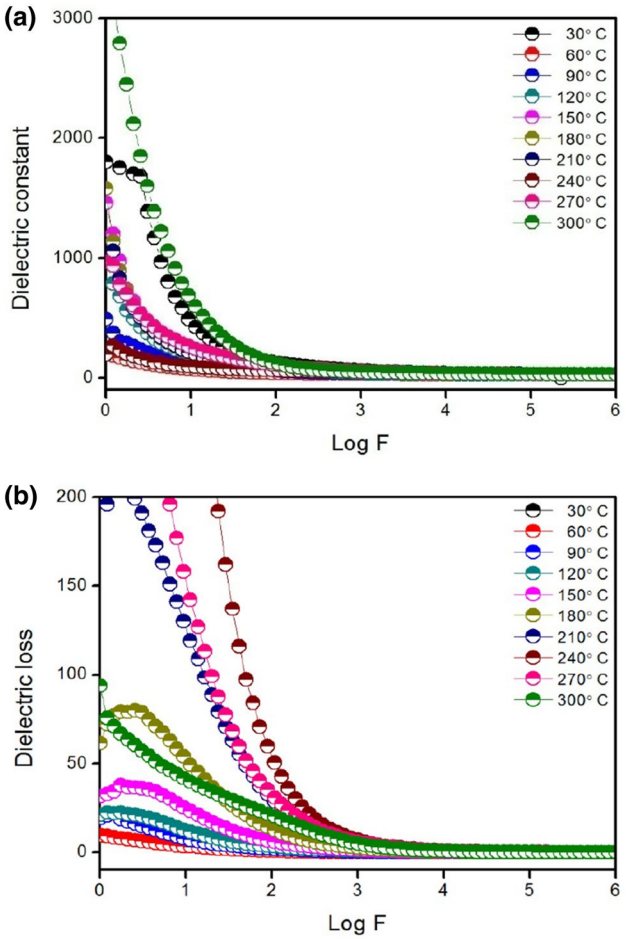

Fig. 8 **a**, **b** Dielectric permittivity and loss spectra of composite CuO/ZnO NPs

other hand, the magnitude of Z″ is found to be maximum at low temperatures and gradual decrease is observed with increase in temperature. The asymmetric peak broadening and average position shift towards high frequency indicates the spread of relaxation time and presence of frequency dependent electrical relaxation in the material. Moreover, Fig. 9c, d demonstrate the complex impedance analysis and analogous equivalent circuit model of the composite CuO/ZnO NPs. A single semicircle arc is observed for all the selective temperature corresponding to the grain boundary effect i.e., parallel combination of grain boundary capacitance and resistance. The reasonable shift of semicircular arc from the zero intercept of the Z′ axis with increase in temperature demonstrates the occurrence of a non-Debye relaxation process. Furthermore, the decrease in the radius of the semicircle arc witnesses the negative temperature coefficient of the resistance type (NTCR) behavior [37]. The simplified equivalent circuit integrates parallel combination of geometric capacitance and layer resistance associated with three series RC elements. In general, the series resistance is related to the contribution from the electrode, whereas the parallel resistance and parallel capacitance are related to the layer resistance and geometric capacitance of the material [35].

4 Conclusions

In summary, the composite CuO/ZnO NPs were prepared by facile precipitation technique. The lower energy gap and near visible region absorption of the composite CuO/ZnO NPs suggest that it could be useful material for visible light driven photocatalyst. The presence of functional groups in the material was identified by FTIR spectral analysis. Powder XRD profile gives only one set of reflection peaks associated with ZnO positions and no traces of reflection peaks corresponds to the CuO, which may be due to the formation of core–shell structured composite CuO/ZnO NPs which is further substantiated from the XPS profile. HRSEM result demonstrates the spherical ZnO NPs are fairly tethered on the dart-like CuO structure and composite CuO/ZnO NPs exhibits slightly agglomerated cluster-like structure. The homogeneous distribution of the product was clearly witnessed by EDS elemental mapping analysis. The photocatalytic activity of material illustrated enhancement of photocatalytic activity against degradation of Rhodamine B and Methylene blue dyes. The dielectric permittivity of the composite CuO/ZnO NPs gives relatively high value and in contrast loss factor gives very low value at lower frequencies than that of CuO and ZnO NPs. This result suggests that the composite CuO/ZnO NPs could be a better applicant for both the photocatalytic activity against organic dyes and microelectronic device fabrications.

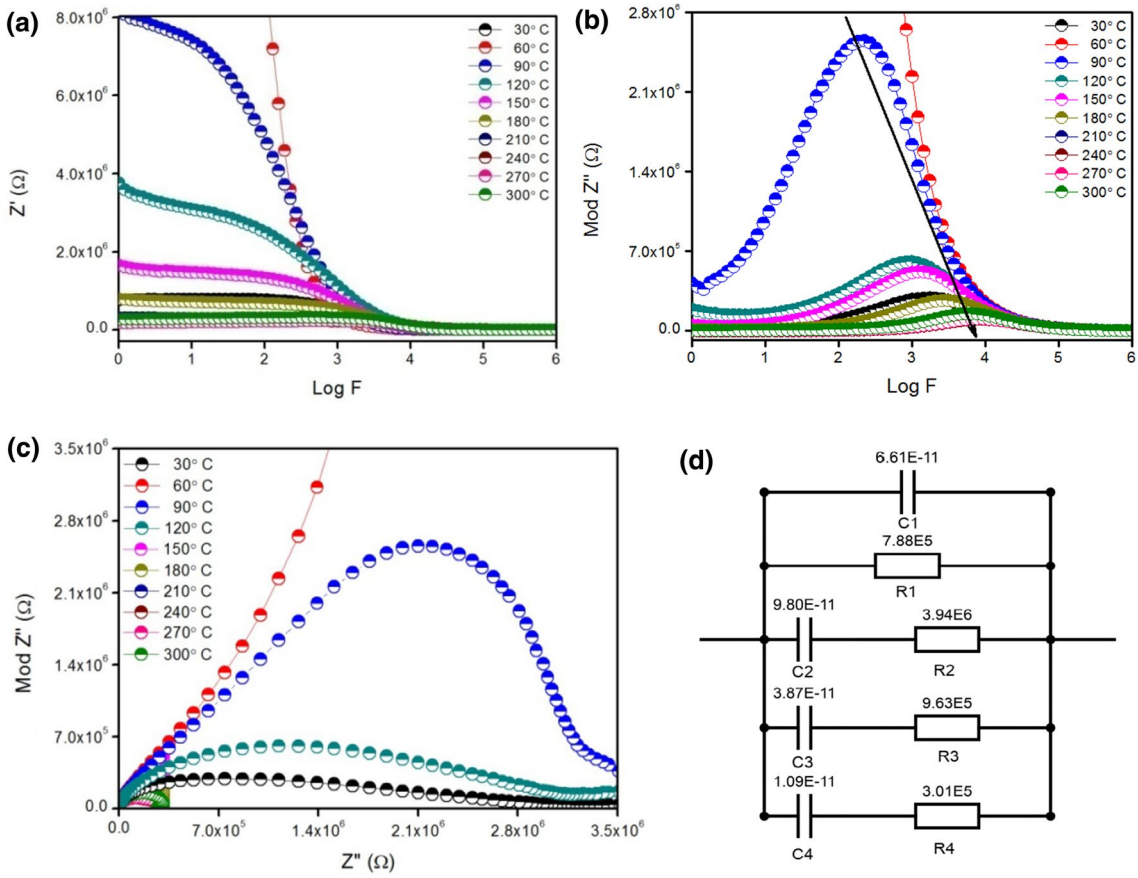

Fig. 9 **a**–**d** Real, imaginary and complex impedance spectra respective equivalent circuit model of composite CuO/ZnO NPs

Acknowledgements The authors are grateful to the Deanship of Scientific Research, King Saud University for funding through Vice Deanship of Scientific Research Chairs.

References

1. Benxia Li, Yanfen Wang, Superlattices Microstruct. **47**, 615–623 (2010)
2. Jing Li, Hezhi Liu, Yu. Yongjun Ji, Guangna Wang Zhang, Yongxia Zhu, Ziyi Zhong, Hu Xiao, Su Fabing, RSC Adv. **6**, 59737–59748 (2016)
3. R. Ghosh Chaudhuri, S. Paria, Chem. Rev. **112**(2012), 2373–2433 (2012)
4. A. Sakthisabarimoorthi, S.A. Martin Britto Dhas, M. Jose, Mater. Sci. Semicond. Process. **71**, 69–75 (2017)
5. A. Sakthisabarimoorthi, S.A. Martin Britto Dhas, M. Jose, Mater. Chem. Phys. **212**, 224–229 (2018)
6. A. Mobeen Amanulla, S.K. Jasmine Shahina, R. Sundaram, C. Maria Magdalane, K. Kaviyarasu, D. Letsholathebe, S.B. Mohamed, J. Kennedy, M. Maaza, J. Photochem. Photobiol., B **183**, 233–241 (2018)
7. C. Maria Magdalane, K. Kaviyarasu, A. Raja, M.V. Arularasu, G.T. Mola, A.B. Isaev, N.A. Al-Dhabi, M.V. Arasu, B. Jeyaraj, J. Kennedy, M. Maaza, J. Photochem. Photobiol., B **185**, 275–282 (2018)
8. C. Maria Magdalane, K. Kaviyarasu, N. Matinise, N. Mayedwa, N. Mongwaketsi, D. Letsholathebe, G.T. Mola, N.A. Al-Dhabi, M. Henini, J. Kennedy, M. Maaza, B. Jeyaraj, S. Afr. J. Chem. Eng. **26**, 49–60 (2018)
9. P. Senthil Kumar, M. Selvakumar, S. Ganesh Babu, S. Induja, S. Karuthapandian, J. Alloys Compd. **701**, 562–573 (2017)
10. Masoud Salavati-Niasari, Fatemeh Davar, Zeinab Fereshteh, Chem. Eng. J. **146**, 498–502 (2009)
11. Noshin Mir, Masoud Salavati-Niasari, Fatemeh Davar, Chem. Eng. J. **181–182**, 779–789 (2012)
12. M. Salavati-Niasari, S.H. Banitaba, J. Mol. Catal. A **201**, 43–54 (2003)
13. Masoud Salavati-Niasari, Parinaz Salemi, Fatemeh Davar, J. Mol. Catal. A **238**, 215–222 (2005)
14. F. Fang, J. Rogers, P.P. Murmu, J. Kennedy, Mod. Phys. Lett. B **32**, 1840067–1840073 (2018)
15. J. Kennedy, P.P. Murmu, E. Manikandan, S.Y. Lee, J. Alloys Compd. **616**, 614–617 (2014)
16. S. Harish, J. Archana, M. Sabarinathan, M. Navaneethan, K.D. Nisha, S. Ponnusamy, C. Muthamizhchelvan, H. Ikeda, D.K. Aswal, Y. Hayakawa, Appl. Surf. Sci. **418**, 103–112 (2017)
17. Mohammadreza Mansournia, Leila Ghaderi, J. Alloys Compd. **691**, 171–177 (2017)
18. K. Mageshwari, D. Nataraj, T. Pal, R. Sathyamoorthy, J. Park, J. Alloys Compd. **625**, 362–370 (2015)
19. J.A. Rodriguez, C.T. Campbell, J. Phys. Chem. **91**, 6648–6658 (1987)

20. J. Hu, W.P. Guo, X.R. Shi, B.R. Li, J.G. Wang, J. Phys. Chem. C **113**, 7227–7235 (2009)
21. G. Fierro, M. LoJacono, M. Inversi, P. Porta, F. Cioci, R. Lavecchia, Appl. Catal. A **137**, 327–348 (1996)
22. Arezoo Shirzadi, Alireza Nezamzadeh-Ejhieh, J. Mol. Catal. A **411**, 222–229 (2016)
23. Xu Linhua, Yang Zhou, Wu Zijun, Gaige Zheng, Jiaojiao He, Yanjing Zhou, J. Phys. Chem. Solids **106**, 29–36 (2017)
24. E.D. Sherly, J.J. Vijaya, L.J. Kennedy, Chin. J. Catal. **36**, 1263–1272 (2015)
25. J. Wang, X.M. Fan, D.Z. Wu, J. Dai, H. Liu, H.R. Liu, Z.W. Zhou, Appl. Surf. Sci. **258**, 1797–1805 (2011)
26. Ruey-Chi Wang, Hsin-Ying Lin, Appl. Phys. A **95**, 813–818 (2009)
27. F. Pola-Albores, W. Antúnez-Flores, P. Amézaga-Madrid, E. Ríos-Valdovinos, M. Valenzuela-Zapata, F. Paraguay-Delgado, M. Miki-Yoshida, J. Cryst. Growth **351**, 77–82 (2012)
28. Hong Li, Linyu Zhu, Mengling Xia, Na Jin, Kaifei Luo, Yahong Xie, Mater. Lett. **174**, 99–101 (2016)
29. R. Saravanan, S. Karthikeyan, V.K. Gupta, G. Sekaran, V. Narayanan, A. Stephen, Mater. Sci. Eng., C **33**, 91–98 (2013)
30. J. Kennedy, P.P. Murmu, J. Leveneur, A. Markwitz, J. Futter, Appl. Surf. Sci. **367**, 52–58 (2016)
31. S. Sagadevan, K. Pal, Z.Z. Chowdhury, J. Mater. Sci. **28**, 12591–12597 (2017)
32. S. Sepulveda-Guzman, B. Reeja-Jayan, E. de la Rosa, A. Torres-Castro, V. Gonzalez-Gonzalez, M. Jose-Yacaman, Mater. Chem. Phys. **115**, 172–178 (2009)
33. Lu Ping, Wei Zhou, Ying Li, Jianchun Wang, Wu Ping, Ceram. Int. **43**, 9798–9805 (2017)
34. H. Zhang, Z. Ji, T. Xia, H. Meng, C. Low-Kam, R. Liu, S. Pokhrel, S. Lin, X. Wang, Y.P. Liao, M. Wang, L. Li, R. Rallo, R. Damoiseaux, D. Telesca, L. Madler, Y. Cohen, J.I. Zink, A.E. Nel, ACS Nano **6**, 4349–4368 (2012)
35. A. Sakthisabarimoorthi, S.A. Martin Britto Dhas, M. Jose, Superlattices Microstruct. **113**, 271–282 (2018)
36. Wen Dong, Dehong Chen, Hu Wanbiao, Terry J. Frankcombe, Hua Chen, Chao Zhou, Fu Zhenxiao, Xiaoyong Wei, Xu Zhuo, Zhifu Liu, Yongxiang Li, Yun Liu, Sci. Rep. **7**, 9950–9956 (2017)
37. A. Sakthisabarimoorthi, S.A. Martin Britto Dhas, R. Robert, M. Jose, Mater. Res. Bull. **106**, 81–92 (2018)